



## Designing Superoleophobic Surfaces

Anish Tuteja, *et al.*

*Science* **318**, 1618 (2007);

DOI: 10.1126/science.1148326

**The following resources related to this article are available online at [www.sciencemag.org](http://www.sciencemag.org) (this information is current as of December 10, 2007):**

**Updated information and services**, including high-resolution figures, can be found in the online version of this article at:

<http://www.sciencemag.org/cgi/content/full/318/5856/1618>

**Supporting Online Material** can be found at:

<http://www.sciencemag.org/cgi/content/full/318/5856/1618/DC1>

This article appears in the following **subject collections**:

Materials Science

[http://www.sciencemag.org/cgi/collection/mat\\_sci](http://www.sciencemag.org/cgi/collection/mat_sci)

Information about obtaining **reprints** of this article or about obtaining **permission to reproduce this article** in whole or in part can be found at:

<http://www.sciencemag.org/about/permissions.dtl>

# Designing Superoleophobic Surfaces

Anish Tuteja,<sup>1</sup> Wonjae Choi,<sup>2</sup> Minglin Ma,<sup>1</sup> Joseph M. Mabry,<sup>3</sup> Sarah A. Mazzella,<sup>3</sup> Gregory C. Rutledge,<sup>1</sup> Gareth H. McKinley,<sup>2\*</sup> Robert E. Cohen<sup>1\*</sup>

Understanding the complementary roles of surface energy and roughness on natural nonwetting surfaces has led to the development of a number of biomimetic superhydrophobic surfaces, which exhibit apparent contact angles with water greater than 150 degrees and low contact angle hysteresis. However, superoleophobic surfaces—those that display contact angles greater than 150 degrees with organic liquids having appreciably lower surface tensions than that of water—are extremely rare. Calculations suggest that creating such a surface would require a surface energy lower than that of any known material. We show how a third factor, re-entrant surface curvature, in conjunction with chemical composition and roughened texture, can be used to design surfaces that display extreme resistance to wetting from a number of liquids with low surface tension, including alkanes such as decane and octane.

Many surfaces in nature, including various plant leaves (1, 2), legs of the water strider (3), troughs on the elytra of desert beetles (4), and geckos' feet (5, 6), are superhydrophobic, displaying apparent contact angles with water (surface tension  $\gamma_{lv} = 72.1$  mN/m) greater than 150° and low contact angle hysteresis. Understanding the complementary roles of the two key surface parameters, surface energy and roughness (7–11), for these materials has led to the development of a number of artificial superhydrophobic surfaces (6, 12, 13). However, superoleophobic surfaces—structured surfaces that resist wetting of liquids with much lower surface tension, such as decane ( $\gamma_{lv} = 23.8$  mN/m) or octane ( $\gamma_{lv} = 21.6$  mN/m)—are extremely rare (14). We have developed several different textured surfaces displaying contact angles greater than 160°, even with octane. This observed superoleophobicity can be explained by considering local surface curvature as the third parameter that affects both the apparent contact angle and hysteresis on any surface. This understanding also allows us to rationalize numerous earlier observations of unexpectedly high liquid repellency on rough surfaces (14–18).

The best-known example of a natural superhydrophobic surface is the surface of the lotus leaf, *Nelumbo nucifera* (1). Numerous studies have suggested that the superhydrophobic character of the lotus leaf surface is attributable to a combination of surface chemistry and roughness on multiple scales. However, a liquid with a markedly lower surface tension, such as hexadecane ( $\gamma_{lv} = 27.5$  mN/m), spreads rapidly across the lotus leaf, leading to a contact angle of  $\sim 0^\circ$  (fig. S8) (19). Such surface oleophilicity can have an impact on a wide range of phenomena, including biofouling by marine

organisms, loss of self-cleaning ability of plant leaves in polluted waters, and swelling of elastomeric seals and O-rings.

Two distinct models, developed independently by Wenzel (7) and Cassie and Baxter [(8), henceforth the Cassie model], are commonly used to explain the effect of roughness on the apparent contact angle of liquid drops (20, 21). The Wenzel model recognizes that surface roughness increases the available surface area of the solid, which modifies the surface contact angle according to the expression

$$\cos \theta^* = r \cos \theta \quad (1)$$

where  $\theta^*$  is the apparent contact angle on the textured surface,  $r$  is the surface roughness, and  $\theta$  is the equilibrium contact angle on a smooth surface of the same material, given by Young's equation (22) as  $\cos \theta = (\gamma_{sv} - \gamma_{sl})/\gamma_{lv}$ , where  $\gamma$  refers to the interfacial tension and the subscripts  $s$ ,  $l$ , and  $v$  refer to the solid, liquid, and vapor phases, respectively.

The Cassie model, on the other hand, postulates that the superhydrophobic nature of a rough surface is caused by microscopic pockets of air remaining trapped below the liquid droplet, leading to a composite interface. If  $\phi_s$  is the fraction of the solid in contact with the liquid, the Cassie equation yields

$$\cos \theta^* = -1 + \phi_s(1 + \cos \theta) \quad (2)$$

In contrast to the Wenzel relation, the Cassie relation allows for the possibility of  $\theta^* > 90^\circ$ , even with  $\theta < 90^\circ$ . Thermodynamic considerations can be used to determine whether a particular textured surface will exist in the Wenzel or the Cassie state [see recent work by Marmur (10) and Nosonovsky (11)]. The situation is somewhat complicated by the presence of multiple local free energy minima leading to so-called "metastable" configurations (2, 10, 23, 24). Indeed, Krupenkin *et al.* (25) have highlighted the possibility of transitioning reversibly between the Wenzel and Cassie states (19). However, careful experimentation with model microstructured surfaces and corresponding free energy calculations show that a series of rough substrates with progressively increasing equilibrium

contact angles exhibits a transition from the Wenzel to the Cassie state (24, 26, 27). The threshold value of the equilibrium contact angle ( $\theta_c$ ) for this transition is obtained by equating Eqs. 1 and 2:

$$\cos \theta_c = (\phi_s - 1)/(r - \phi_s) \quad (3)$$

Because  $r > 1 > \phi_s$ , the critical value of the equilibrium contact angle  $\theta_c$  for this transition is necessarily greater than 90°. Thus, it may be anticipated that for  $\theta < 90^\circ$ , a surface cannot exist in the Cassie state or that the creation of highly nonwetting surfaces ( $\theta^* \gg 90^\circ$ ) requires  $\theta > \theta_c > 90^\circ$ . These arguments highlight the difficulty of developing surfaces for which  $\theta^* > 150^\circ$  when in contact with alkanes such as decane or octane, as there are no reports of a natural or artificial surface with a low enough surface energy (19) to enable  $\theta > 90^\circ$  with these liquids (14–17, 28).

However, studies on leaves of plants such as *Cotinus coggygria* and *Ginkgo biloba* suggest the possibility of designing textured surfaces with unexpectedly high nonwetting properties. Herminghaus (2) first pointed out that these leaves display superhydrophobic properties, even with  $\theta < 90^\circ$ . Indeed, recent experiments show that even the wax on the lotus leaf surface is weakly hydrophilic with  $\theta \approx 74^\circ$  (29). The superhydrophobic state of these textured surfaces is not the true equilibrium state, and submerging the leaf in water to a certain depth can cause a transition from this metastable Cassie state to the Wenzel state. Correspondingly, it may be possible to design metastable superoleophobic surfaces even though we are limited to materials with  $\theta < 90^\circ$ .

We have synthesized a class of hydrophobic polyhedral oligomeric silsesquioxane (POSS) molecules in which the rigid silsesquioxane cage is surrounded by perfluoro-alkyl groups (inset, Fig. 1A). A number of molecules with different organic groups including 1H,1H,2H,2H-heptadecafluorodecyl (referred to as fluorodecyl POSS) and 1H,1H,2H,2H-tridecafluorooctyl (fluorooctyl POSS) were synthesized. We refer to this class of materials generically as fluoroPOSS (19). The high surface concentration and surface mobility of  $-CF_2$  and  $-CF_3$  groups, together with the relatively high ratio of  $-CF_3$  groups with respect to  $-CF_2$  groups, results in a very hydrophobic material with low surface energy. A film of fluorodecyl POSS, spin-coated on a Si wafer, has an advancing ( $\theta_{adv}$ ) and receding ( $\theta_{rec}$ ) contact angle of  $124.5^\circ \pm 1.2^\circ$ , with a root mean square (RMS) roughness  $r_q = 3.5$  nm.

By varying the mass fraction of specific fluoroPOSS molecules blended with a polymer, we can systematically change  $\gamma_{sv}$  for the polymer-fluoroPOSS blend. We studied blends of a moderately hydrophilic polymer, poly(methyl methacrylate) (PMMA), and fluorodecyl POSS (which had the lowest surface energy of the POSS molecules synthesized). Varying the mass fraction of fluo-

<sup>1</sup>Department of Chemical Engineering, Massachusetts Institute of Technology, Cambridge, MA 02139, USA. <sup>2</sup>Department of Mechanical Engineering, Massachusetts Institute of Technology, Cambridge, MA 02139, USA. <sup>3</sup>Air Force Research Laboratory, Edwards Air Force Base, CA 93524, USA.

\*To whom correspondence should be addressed. E-mail: gareth@mit.edu (G.H.M.); rechen@mit.edu (R.E.C.)

rodecyl POSS systematically changed both  $\theta_{adv}$  and  $\theta_{rec}$  for water on spin-coated films of PMMA and fluorodecyl POSS (Fig. 1A). The atomic force microscope (AFM) phase images of the spin-coated surfaces, as well as the shapes of water droplets (volume  $\approx 2 \mu\text{l}$ ) on those surfaces, are shown in Fig. 1B. Comparing the phase images of the pure PMMA and 1.9 weight % fluorodecyl POSS indicates substantial surface migration of POSS during solvent evaporation, as would be expected because of its low surface energy (30, 31).

The corresponding rough fluorodecyl POSS-PMMA surfaces are created by electrospinning (32–34). In Fig. 1C we show the advancing ( $\theta_{adv}^*$ ) and receding ( $\theta_{rec}^*$ ) contact angles with water for the various electrospun surfaces. The inset shows the “beads on a string” (35) morphology of a representative fiber mat, as well as the multiple scales of roughness and high porosity generated by the electrospinning process. There is no observable change in the micrometer-scale structure with increasing mass fraction of POSS as viewed with a scanning electron microscope (SEM). X-ray photoelectron spectroscopy (XPS) analysis indicates substantial

surface migration of the fluoroPOSS molecules during electrospinning (fig. S9). The surfaces become superhydrophobic (movie S1) for all POSS concentrations above  $\sim 10$  weight % ( $\theta_{adv}^* = \theta_{rec}^* = 161^\circ \pm 2^\circ$ ).

An important observation from Fig. 1C is that  $\theta_{adv}^* > 90^\circ$  for pure PMMA and 1.9 weight % POSS-PMMA electrospun surfaces, even though in each case  $\theta_{adv} < 90^\circ$  (Fig. 1A). This is surprising, because for  $\theta < 90^\circ$  the rough surfaces are expected to be in the Wenzel state, and from Eq. 1 we expect  $\theta_{adv}^* < \theta_{adv}$ . This unusual effect is further explored in the form of the general wetting diagram (13) in Fig. 1D, which shows a plot of  $\cos \theta_{adv}^*$  and  $\cos \theta_{rec}^*$  on the rough electrospun surfaces as a function of  $\cos \theta_{adv}$  and  $\cos \theta_{rec}$  for the corresponding smooth (spin-coated) surfaces. Even at low POSS concentrations ( $< 2$  weight %), the surfaces display high apparent advancing contact angles indicative of being in the Cassie state. However, these textured surfaces also exhibit high contact angle hysteresis. Separate experiments show that this Cassie state is metastable, as water droplets released from a height can penetrate and wet the fiber mat.

The electrospun fibers similarly display extremely oleophobic properties ( $\theta^* \gg 90^\circ$ ), even though all of the corresponding spin-coated surfaces are oleophilic ( $\theta < 90^\circ$ ). Plots of  $\theta_{adv}^*$  and  $\theta_{rec}^*$  for hexadecane and decane (Fig. 2, A and B) show that in many cases both  $\theta_{adv}^*$  and  $\theta_{rec}^*$  for the electrospun surfaces are much greater than  $90^\circ$ , and a transition from the Wenzel to the metastable Cassie state can also be observed for each alkane. This metastable state is related to a local minimum in free energy (19) that systematically shifts to higher POSS concentrations (lower surface energy) with decreasing liquid surface tension. The electrospinning process also enables fibers to be deposited on fragile or natural surfaces (such as a lotus leaf) to confer oleophobicity in addition to superhydrophobicity (fig. S8).

The advancing contact angles for various liquid alkanes on the electrospun and spin-coated surfaces can be combined to form a master curve of  $\theta_{adv}^*$  versus  $\theta_{adv}$  (Fig. 2C). A sharp transition from the Wenzel state to the nonwetting Cassie state is observed at an equilibrium contact angle of  $\theta_c \approx 69^\circ$  (see also fig. S10). This value of  $\theta_c$  depends on the free

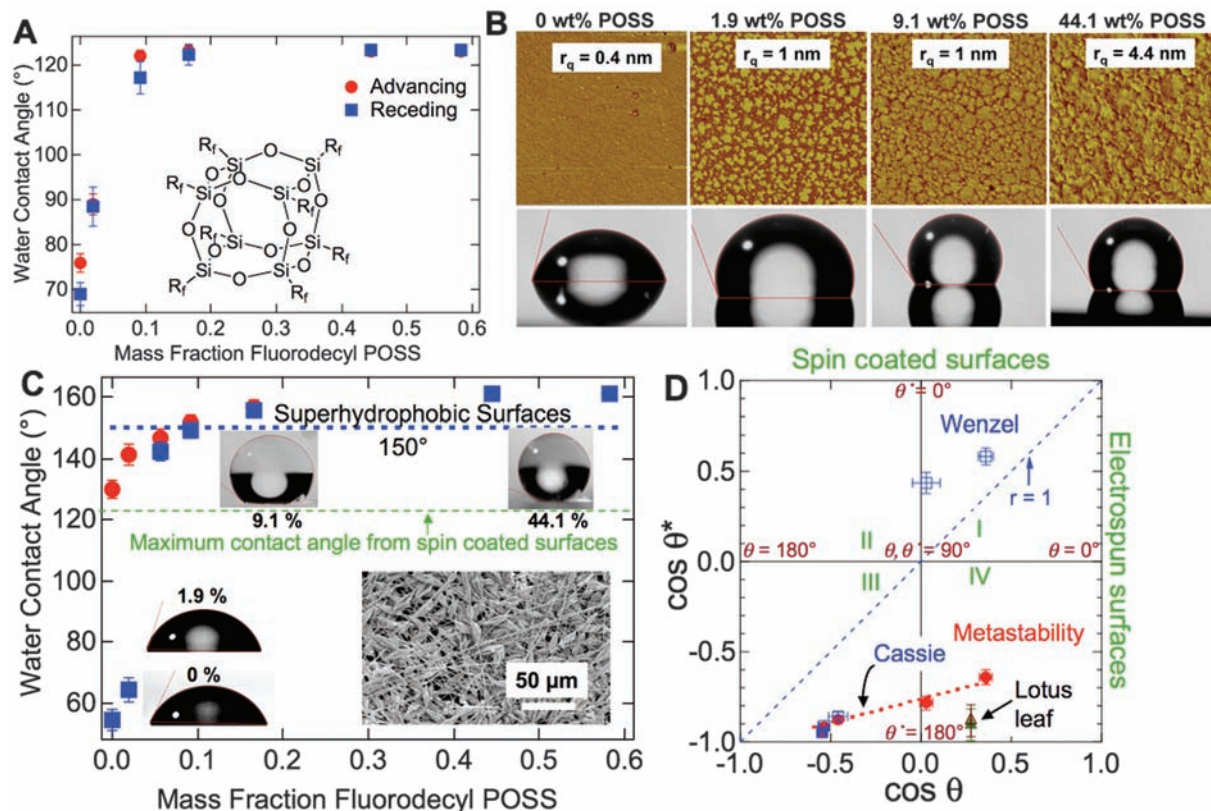


**Fig. 1.** Tunable hydrophobicity of fluoroPOSS-PMMA blends. **(A)**  $\theta_{adv}$  and  $\theta_{rec}$  for water as a function of the mass fraction of fluorodecyl POSS. The inset shows the general molecular structure of fluoroPOSS molecules. The alkyl chains ( $R_f$ ) have the general molecular formula  $-\text{CH}_2\text{CH}_2(\text{CF}_2)_n\text{CF}_3$ , where  $n = 0, 3, 5, \text{ or } 7$ . **(B)** The phase angle scale on the AFM images is  $0^\circ$  to  $10^\circ$  for the 0, 9.1, and 44.1 weight % POSS images and  $0^\circ$  to  $90^\circ$  for the 1.9 weight % POSS image. The RMS roughness ( $r_q$ ) for each film is also given. By comparison,  $r_q$  for a Si wafer is  $\sim 0.2 \text{ nm}$ . **(C)**  $\theta_{adv}^*$  (red dots) and  $\theta_{rec}^*$  (blue

squares) for water on the electrospun surfaces. The inset shows a SEM micrograph for an electrospun surface containing 9.1 weight % POSS. The maximum contact angle for water on the spin-coated surfaces is also shown. **(D)** Plot of  $\cos \theta_{adv}^*$  (solid red dots) and  $\cos \theta_{rec}^*$  (open blue squares) for water as a function of  $\theta_{adv}$  and  $\theta_{rec}$ . The surfaces in the lower right quadrant (IV) of this diagram correspond to hydrophilic substrates that are rendered hydrophobic purely by topography. The advancing and receding contact angles for the lotus leaf (solid and open triangles, respectively) are also provided for comparison.

energy landscape separating the Cassie and Wenzel states (19) and will be dependent on the topography of the surfaces under consideration; however, it is clear from Fig. 2C and fig. S10 that  $\theta_c$  can be considerably less than  $90^\circ$ .

The robustness of the metastable Cassie state for the electrospun fiber surfaces is determined by measuring the height of liquid (or static pressure) required for forcing the liquid through the fibers (denoted  $h^*$ ). The surfaces do not transition to the Wenzel state even when submerged under 150 mm of hexadecane. To scale such observations, we use the characteristic capillary rise height

$$h_{\text{cap}} = 2\gamma_{\text{lv}} \cos \theta / \rho g D \quad (4)$$

for the porous substrate, where the relevant capillary pore size  $2D$  is the average edge-to-edge spacing of the nanofibers (Fig. 3A) (8),  $\rho$  is the fluid density, and  $g$  is the acceleration due to gravity. In Fig. 2D we plot the normalized breakthrough pressure

$$h^*/h_{\text{cap}} = \rho g D h^* / (2\gamma_{\text{lv}} \cos \theta) \quad (5)$$

required to wet a fiber mat containing 44 weight % POSS. Calculations shown in (19) yield the pres-

sure required to increase the curvature of a liquid droplet until it impinges on the next level of fibers. These pressures (normalized with the capillary pressure) are also shown in Fig. 2D.

An extremely useful application for these porous electrospun materials can be deduced by noticing that many of the electrospun sur-

faces with low POSS concentrations are both superhydrophobic and superoleophobic ( $\theta_{\text{alkane}}^* \approx 0^\circ$ ). Thus, these surfaces are ideal for separating mixtures or dispersions of alkanes (oils) and water (36), as shown in Fig. 2E.

It is the local surface curvature that plays a key role in driving the oleophobicity of electro-

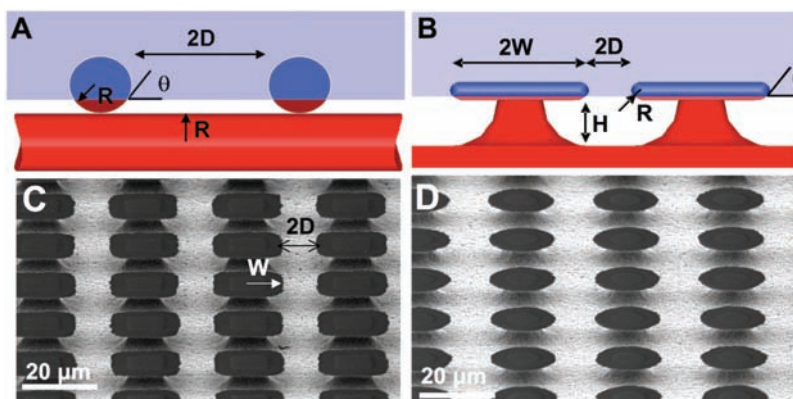


**Fig. 3.** Critical role of re-entrant curvature. (A and B) Cartoons highlighting the formation of a composite interface on surfaces with re-entrant topography (for both fibers and micro-hoods). The geometric parameters  $R$ ,  $D$ ,  $H$ , and  $W$  characterizing these surfaces are also shown. The blue surface is wetted while the red surface remains nonwetted when in contact with a liquid whose equilibrium contact angle is  $\theta$  ( $< 90^\circ$ ). (C and D) SEM micrographs for two micro-hoodoo surfaces having square and circular flat caps, respectively. The samples are viewed from an oblique angle of  $30^\circ$ .

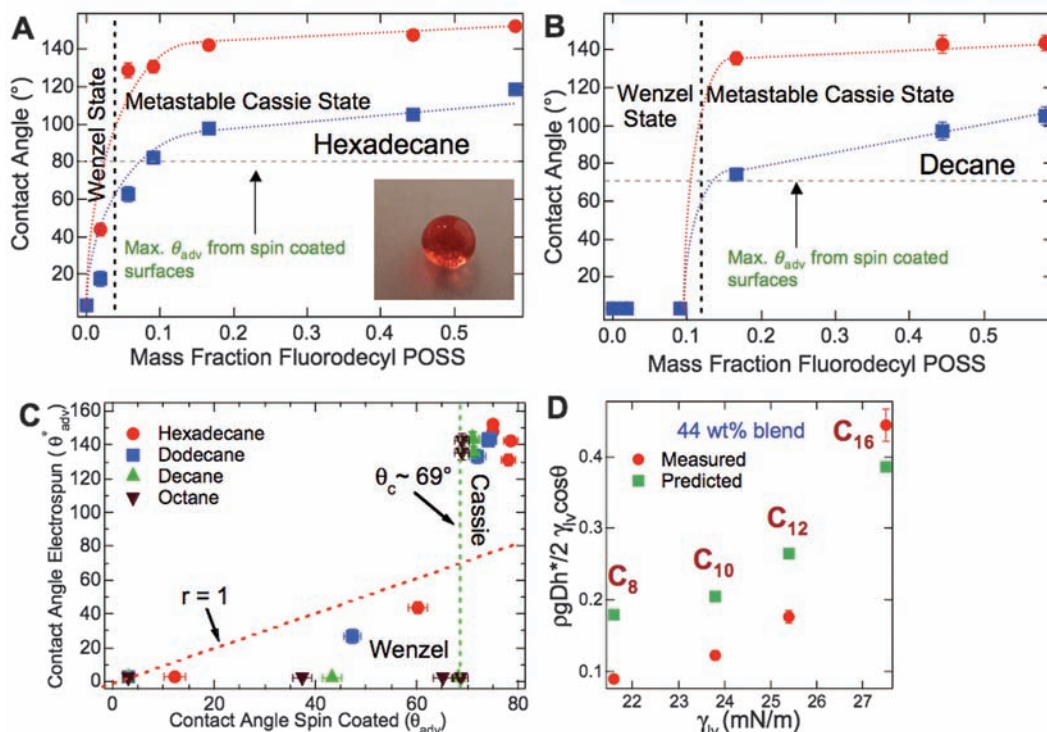
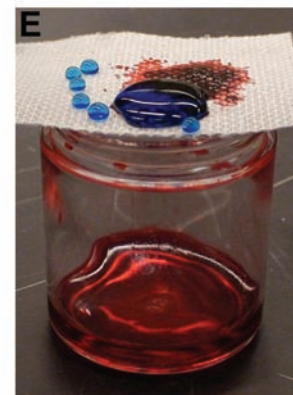


**Fig. 2.** (A and B)  $\theta_{\text{adv}}^*$  (red dots) and  $\theta_{\text{rec}}^*$  (blue squares) for hexadecane and decane, respectively, on the electrospun surfaces. The maximum contact angles on corresponding spin-coated surfaces ( $\theta_{\text{adv}}$ ) are also shown. The inset of (A) shows a drop of hexadecane (dyed with Oil Red O) on a 44 weight % fluorodecyl POSS electrospun surface. (C)  $\theta_{\text{adv}}^*$  for hexadecane, dodecane, decane, and octane as a function of  $\theta_{\text{adv}}$ . (D) Normalized breakthrough pressure required to transition irreversibly from the metastable Cassie to the Wenzel

state on the surface of fibers containing 44 weight % fluorodecyl POSS. Our predictions for the breakthrough pressure (19) using  $R = 500$  nm and  $D = 4$   $\mu\text{m}$  are also shown. (E) A steel grid (square pores with 1-mm spacing) coated with electrospun fibers containing 9.1 weight % fluorodecyl POSS used for oil-water separation. Octane droplets (colored with Oil Red O) easily pass through the membrane, whereas water droplets (dyed with methylene blue) bead up on the surface (see movie S2).



spun fibers. To support this thesis, we fabricated model re-entrant structures (i.e., surfaces having concave topographic features) of the form shown in Fig. 3, B to D. These structures were fabricated on flat Si wafers by means of SiO<sub>2</sub> deposition followed by a two-step etching process comprising reactive ion etching of SiO<sub>2</sub> and subsequent isotropic etching of Si with the use of vapor-phase XeF<sub>2</sub> (19). This results in undercut silicon pillars (covered with a 300-nm layer of SiO<sub>2</sub>) and troughs. Because of their similarity to geomorphological features, we refer to these structures as micro-hoodoos (37). A key design feature of both of the electrospun fiber and hoodoo surfaces is that they possess re-entrant curvature, in addition to exhibiting both the desired characteristics of “roughness” (i.e.,  $r > 1$ ) and low wetted surface fraction (i.e.,  $\phi_s < 1$ ) embodied in Eqs. 1 and 2.

The flat liquid-air interface shown schematically in Fig. 3, A and B (38) is in contact with the electrospun fibers and the micro-hoodoos. As a direct result of re-entrant curvature, for any value of  $0^\circ < \theta < 180^\circ$ , each surface in Fig. 3, A and B, provides a point somewhere along the fiber or cap length at which Young’s equation is satisfied locally at the air-liquid-solid interface (10, 11, 34). This is in contrast to other common patterned supports [e.g., arrays of vertical posts (25)], which can form a composite interface and satisfy the Young equation only if  $\theta > 90^\circ$ . It is therefore possible to form a composite interface on re-entrant curved surfaces, with the drop sitting partially on air, and thus have  $\theta^* \gg 90^\circ$  even with  $\theta < 90^\circ$ . However, this Cassie state is only locally stable, because the total energy of the system decreases appreciably (19) if the liquid advances and completely covers the

fibers/hoodoos, leading to a fully wetted interface (11, 39).

Analysis of these re-entrant geometries yields two important design parameters (19). For the electrospun fibers, the first is the spacing ratio  $D^* = (R + D)/R$  (where  $R$  is the radius of the fibers), which directly affects  $\phi_s$  (8) and thus the apparent contact angle. The second is the robustness parameter  $H^* = 2(1 - \cos \theta)Rl_{\text{cap}}/D^2$  [where  $l_{\text{cap}} = (\gamma_{\text{lv}}/\rho g)^{1/2}$ ], which measures the robustness of the metastable Cassie state with respect to the fluid properties, equilibrium contact angle, and surface geometry. Varying the  $R$  and  $D$  values of these structures has competing effects on the apparent contact angles and the stability of the composite interface. Thus, the metastable Cassie state may not be accessible in practice on every surface that possesses re-entrant curvature, depending on the applied pressure required to transition irreversibly from the metastable Cassie to the Wenzel state. However, it is clear that to maximize both  $\theta^*$  and the stability of the Cassie state, we seek sparsely spaced, highly re-entrant surfaces with both  $H^* \gg 1$  and  $D^* \gg 1$ . This is why our electrospun mats of nanofibers ( $D^* = 9$ ;  $H^* = 46$  for octane on fibers containing 44.1 weight % POSS) provide a more robust Cassie state than do prototypical wire gratings (8) ( $D^* = 1.9$  to 5.8;  $H^* = 0.76$  to 7.6 for octane), even at higher pressures.

Evaluating the magnitudes of these dimensionless design parameters also helps explain the oleophobicity observed for aggregates of anodized alumina (15, 16), plasma-treated cotton fibers (14), and spherical arrays of poly(tetrafluoroethylene) (PTFE) particles (17), as well as superhydrophobicity obtained on a

hydrophilic substrate with a “popcorn-like” morphology (18). Re-entrant structures on the lotus leaf surface, in the form of “overhangs” (2, 40) on the hemispherical nubs (inset, fig. S8A), are also the reason for its unexpectedly high hydrophobicity.

For the micro-hoodoo geometry, the design parameters take the form  $D^* = [(W + D)/W]^2$  and  $H^* = 2[(1 - \cos \theta)R + H]l_{\text{cap}}/D^2$ . Because the hoodoo spacing ( $W$ ) and height ( $H$ ) can be varied independently for these surfaces (Fig. 3B), we can easily decouple variations in  $D^*$  and  $H^*$  and thus engineer surfaces with both higher apparent contact angles and much greater robustness than even the electrospun fibers can provide.

During the patterning and etching process for fabricating the micro-hoodoos, we also left untextured areas, thus enabling the measurement of both  $\theta$  and  $\theta^*$  on the same wafer. For water on the textured surfaces (Fig. 4A), re-entrant curvature in the absence of any chemical surface treatment leads to  $\theta_{\text{adv}}^* \approx 143^\circ$  ( $\theta_{\text{rec}}^* \approx 104^\circ$ ;  $D^* = 2.3$ ). By comparison, for water on the smooth portion of the same wafer,  $\theta_{\text{adv}} \approx 10^\circ$ . The robustness of the metastable Cassie state on the SiO<sub>2</sub> micro-hoodoo surface (with  $H^* = 1560$  for water) is illustrated in Fig. 4B. The re-entrant surface resists both the advancing (41) and receding of the water droplet. The images of the receding droplet also highlight the high hysteresis ( $\Delta\theta^* \approx 39^\circ$ ) on the textured surface; however, it is clear that the water droplet has not reached the SiO<sub>2</sub> surface at the base of the hoodoos, in which case it would have been impossible to withdraw the water droplet completely.

The SiO<sub>2</sub> hoodoos were then treated with vapor-phase 1H,1H,2H,2H-perfluorodecyltrichlorosilane to lower  $\gamma_{\text{sv}}$  chemically and hence combine low surface energy with re-entrant surface curvature. The advancing and receding contact angles for octane on the silanized hoodoo surfaces ( $D^* = 2.3$  to 9;  $H^* = 64$  to 1040 for octane) are shown in Fig. 4C as a function of  $\phi_s$  or  $1/D^*$ . The inset of Fig. 4C shows a drop of octane on a silanized micro-hoodoo surface ( $\phi_s = 0.11$ ,  $D^* = 9$ ,  $H^* = 64$ ;  $\theta_{\text{adv}}^* \approx 163^\circ$ ,  $\theta_{\text{rec}}^* \approx 145^\circ$ ). A 10- $\mu\text{l}$  drop of octane can easily be rolled off this surface by tilting to  $15^\circ$ . Corresponding measurements for octane on a smooth SiO<sub>2</sub> surface ( $r_q \approx 0.5$  nm) covered with the same silane coating yielded only  $\theta_{\text{adv}} \approx 55^\circ$ ,  $\theta_{\text{rec}} \approx 50^\circ$ . The contact angles monotonically increased with decreasing wetted area fraction  $\phi_s$ . This is in broad agreement with Eq. 2 (42) and results from the variable resistance offered to the receding meniscus, which is expected to be proportional to the total number of re-entrant structural elements at the air-liquid-solid three-phase contact line. Silanized micro-hoodoos with  $\phi_s = 0.03$  ( $D^* = 36$ ,  $H^* = 10$ ) are fully wetted by octane.

We have demonstrated two different approaches for fabricating surfaces possessing re-entrant curvature. In each case, the re-entrant textures allow for the possibility of constructing extremely nonwetting surfaces that can support

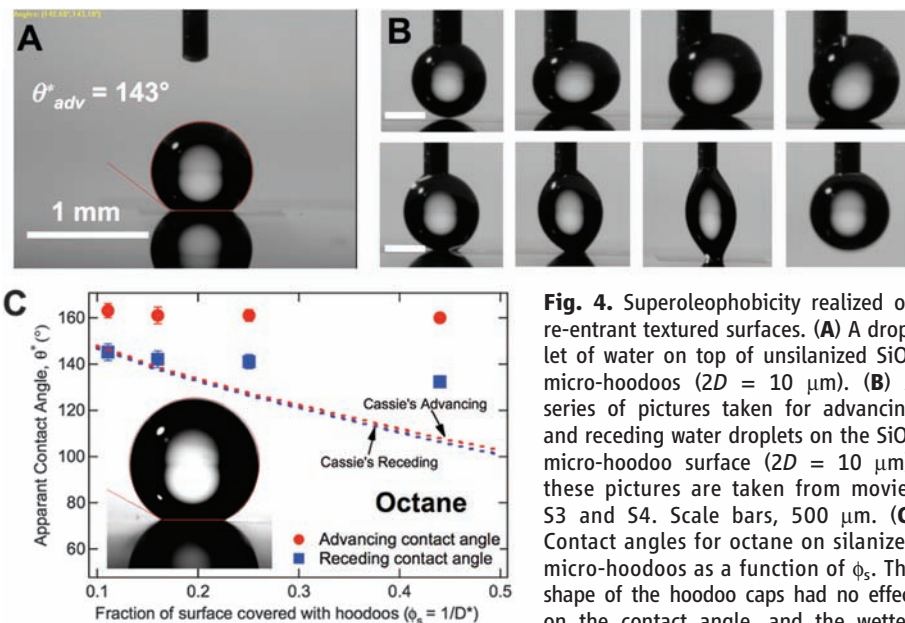


**Fig. 4.** Superoleophobicity realized on re-entrant textured surfaces. (A) A droplet of water on top of unsilanized SiO<sub>2</sub> micro-hoodoos ( $2D = 10 \mu\text{m}$ ). (B) A series of pictures taken for advancing and receding water droplets on the SiO<sub>2</sub> micro-hoodoo surface ( $2D = 10 \mu\text{m}$ ); these pictures are taken from movies S3 and S4. Scale bars,  $500 \mu\text{m}$ . (C) Contact angles for octane on silanized micro-hoodoos as a function of  $\phi_s$ . The shape of the hoodoo caps had no effect on the contact angle, and the wetted area fraction  $\phi_s$  was found to be the only

important parameter. Predictions from the Cassie equation (8) are also included for comparison (dashed lines).

the Cassie state with water and various organic liquids. The presence of re-entrant curvature, though, is not a sufficient condition for developing highly nonwetting surfaces; the Cassie state may be inaccessible in practice if the applied pressure (or energy barrier) required to transition from the Cassie to the Wenzel state is small. However, by independently controlling both the chemical and topographic nature of surfaces (as embodied in two dimensionless design parameters,  $D^*$  and  $H^*$ ), we have shown that it is possible to design extremely robust nonwetting surfaces.

#### References and Notes

- W. Barthlott, C. Neinhuis, *Planta* **202**, 1 (1997).
- S. Herminghaus, *Europhys. Lett.* **52**, 165 (2000).
- X. Gao, L. Jiang, *Nature* **432**, 36 (2004).
- A. R. Parker, C. R. Lawrence, *Nature* **414**, 33 (2001).
- K. Autumn *et al.*, *Nature* **405**, 681 (2000).
- J. Genzer, K. Efimenko, *Biofouling* **22**, 339 (2006).
- R. N. Wenzel, *Ind. Eng. Chem.* **28**, 988 (1936).
- A. B. D. Cassie, S. Baxter, *Trans. Faraday Soc.* **40**, 546 (1944).
- M. Callies, D. Quere, *Soft Mat.* **1**, 55 (2005).
- A. Marmur, *Langmuir* **19**, 8343 (2003).
- M. Nosonovsky, *Langmuir* **23**, 3157 (2007).
- A. Nakajima, K. Hashimoto, T. Watanabe, *Monatsh. Chem.* **132**, 31 (2001).
- D. Quere, *Rep. Prog. Phys.* **68**, 2495 (2005).
- S. R. Coulson, I. S. Woodward, J. P. S. Badyal, S. A. Brewer, C. Willis, *Chem. Mater.* **12**, 2031 (2000).
- K. Tsujii, T. Yamamoto, T. Onda, S. Shibuichi, *Angew. Chem. Int. Ed. Engl.* **36**, 1011 (1997).
- S. Shibuichi, T. Yamamoto, T. Onda, K. Tsujii, *J. Colloid Interface Sci.* **208**, 287 (1998).
- W. Chen *et al.*, *Langmuir* **15**, 3395 (1999).
- M. Zhu, W. Zuo, H. Yu, W. Yang, Y. Chen, *J. Mater. Sci.* **41**, 3793 (2006).
- See supporting material on Science Online.
- L. Gao, T. J. McCarthy, *Langmuir* **23**, 3762 (2007).
- Recent work by McCarthy and colleagues (20) points out that these models are applicable only at the solid-liquid-vapor three-phase contact line (drop perimeter) and that the interfacial area within the drop perimeter does not affect either the apparent contact angle or the hysteresis; thus, these models can be easily applied only to surfaces with a homogeneous texture, as considered here.
- T. Young, *Philos. Trans. R. Soc. London* **95**, 65 (1805).
- N. A. Patankar, *Langmuir* **19**, 1249 (2003).
- B. He, N. A. Patankar, J. Lee, *Langmuir* **19**, 4999 (2003).
- T. N. Krupenkin *et al.*, *Langmuir* **23**, 9128 (2007).
- L. Barbieri, E. Wagner, P. Hoffmann, *Langmuir* **23**, 1723 (2007).
- A. Lafuma, D. Quere, *Nat. Mater.* **2**, 457 (2003).
- W. A. Zisman, in *Contact Angle, Wettability and Adhesion*, F. M. Fowkes, Ed. (American Chemical Society, Washington, DC, 1964), pp. 1–51.
- Y.-T. Cheng, D. E. Rodak, *Appl. Phys. Lett.* **86**, 144101 (2005).
- D. E. Suk *et al.*, *Macromolecules* **35**, 3017 (2002).
- D. H. K. Pan, W. M. Prest Jr., *J. Appl. Phys.* **58**, 2861 (1985).
- D. H. Reneker, A. L. Yarin, H. Fong, S. Koombhongse, *J. Appl. Phys.* **87**, 4531 (2000).
- M. Ma, Y. Mao, M. Gupta, K. K. Gleason, G. C. Rutledge, *Macromolecules* **38**, 9742 (2005).
- M. Ma *et al.*, *Adv. Mater.* **19**, 255 (2007).
- H. Fong, I. Chun, D. H. Reneker, *Polym.* **40**, 4585 (1999).
- L. Feng *et al.*, *Angew. Chem.* **116**, 2046 (2004).
- These surfaces are referred to as micro-hoodoos because their geometry and process of creation are reminiscent of geological features called hoodoos, which are created by soil erosion. Hoodoos are composed of a soft sedimentary rock topped by a piece of harder, less easily eroded stone.
- Because  $2D \ll (\gamma_{lv}/\rho g)^{0.5}$  (capillary length;  $\rho$  is the density of liquid), the effect of gravity is negligible and we approximate the liquid-air interface to be a horizontal plane.
- Nosonovsky (11) recently derived another important criterion for the creation of a local minimum in free energy, and thus for the creation of a stable heterogeneous interface:  $dA_{st}d\theta < 0$ , where  $dA_{st}$  is the change in solid-liquid contact area with the advancing or receding of the liquid, and  $d\theta$  is the change in local contact angle. This criterion also emphasizes the importance of re-entrant surfaces.
- L. Cao, H. H. Hu, D. Gao, *Langmuir* **23**, 4310 (2007).
- As the surface is pushed toward the water droplet, the droplet moves, and hence the normal force is not transferred perfectly.
- The difference in contact angle values from the Cassie prediction is related to contact line pinning.
- Supported by Air Force Research Laboratory contract FA9300-06M-T015 and Air Force Office of Scientific Research contracts FA9550-07-1-0272 and LRIR-92PLOCOR, with additional student support provided by the NSF Nanoscale Interdisciplinary Research Team on Nanoscale Wetting (DMR-0303916). We thank the Institute for Soldier Nanotechnologies at MIT for the use of facilities.

#### Supporting Online Material

www.sciencemag.org/cgi/content/full/318/5856/1618/DC1

Materials and Methods

SOM Text

Figs. S1 to S10

Tables S1 to S3

References

Movies S1 to S4

25 July 2007; accepted 22 October 2007

10.1126/science.1148326

## The Equatorial Ridges of Pan and Atlas: Terminal Accretionary Ornaments?

Sébastien Charnoz,<sup>1\*</sup> André Brahic,<sup>1</sup> Peter C. Thomas,<sup>2</sup> Carolyn C. Porco<sup>3</sup>

In the outer regions of Saturn's main rings, strong tidal forces balance gravitational accretion processes. Thus, unusual phenomena may be expected there. The Cassini spacecraft has recently revealed the strange "flying saucer" shape of two small satellites, Pan and Atlas, located in this region, showing prominent equatorial ridges. The accretion of ring particles onto the equatorial surfaces of already-formed bodies embedded in the rings may explain the formation of the ridges. This ridge formation process is in good agreement with detailed Cassini images showing differences between rough polar and smooth equatorial terrains. We propose that Pan and Atlas ridges are kilometers-thick "ring-particle piles" formed after the satellites themselves and after the flattening of the rings but before the complete depletion of ring material from their surroundings.

In images sent by the Voyager spacecraft in the early 1980s, two small satellites were discovered orbiting inside Saturn's rings (1, 2), where Roche (3) had shown that strong tidal forces prevent the formation of any big satellite. Pan is located in the A ring's Encke Gap at

133,600 km from Saturn's center, and Atlas orbits at 137,700 km from Saturn's center, just outside the A ring. The Cassini spacecraft has recently resolved them both. Their shapes (Fig. 1) are close to oblate ellipsoids, with equatorial radii of 16.5 and ~19.5 km, and polar radii of ~10.5 km and 9 km for Pan and Atlas, respectively. These dimensions (4) are close to the moons' Hill radii (corresponding to the satellites' gravitational cross sections). More unexpectedly, both have a prominent equatorial ridge. These ridges are roughly symmetric about the bodies' equators and give them the appearance of a "flying saucer." Assuming that Pan and Atlas

are rotating synchronously around Saturn (like the Moon around the Earth), consistent with Cassini images taken at several different times (5), Pan's ridge extends from  $-15^\circ$  to  $+15^\circ$  latitude ( $\pm \sim 5^\circ$ ) and apparently entirely encircles the satellite. Atlas' ridge extends from  $-30^\circ$  to  $+30^\circ$  latitude ( $\pm 10^\circ$ ) on the trailing side, whereas on the leading side the ridge is much less prominent, with a modest depression on the leading side near the equator (4) (Fig. 1C).

Recent work (6) has shown that a fast rotation may explain the diamond shape of the near-earth asteroid 1999 KW4 because of the balance of the centrifugal and gravity forces at the asteroid's equator. This mechanism seems, however, inadequate to explain the shapes of Pan and Atlas: Their rotation periods  $T$  (~14 hours) are much too long for centrifugal forces to balance surface gravity (which requires  $T \sim 5$  hours). In addition, Saturn's tidal stress would elongate the moons in the radial direction (3, 7) rather than create an equatorial ridge. Therefore, neither centrifugal nor tidal forces seem adequate to explain these ridges.

A number of circumstances led us to investigate a different scenario for the creation of the ridges: (i) Contrary to other resolved satellites, Pan and Atlas are embedded in Saturn's rings. (ii) The ridges are equatorial and precisely in the same plane as Saturn's rings. (iii) The vertical motion of Atlas (and perhaps Pan) through the rings is approximately equal to the

<sup>1</sup>Laboratoire AIM, Commissariat à l'Énergie Atomique (CEA)/Université Paris 7/CNRS, 91191 Gif-sur-Yvette Cedex, France.

<sup>2</sup>Center for Radiophysics and Space Research, Cornell University, Ithaca, NY 14853, USA. <sup>3</sup>Cassini Imaging Central Laboratory for Operations, Space Science Institute, Boulder, CO 80301, USA.

\*To whom correspondence should be addressed: charnoz@cea.fr